Available online at www.sciencedirect.com
ScienceDirect
Trans. Nonferrous Met. Soc. China 33(2023) 2898−2912
Transactions of Nonferrous Metals Society of China
www.tnmsc.cn

Microstructure and properties of Al−2Mg−0.5Mn alloy with narrow crystallization temperature range realized by adding trace elements

Meng-jia LI[1], En-gui ZHANG[2], Shu-yu LIU[1], Xiang-dong WANG[3], Yun-jia SHI[4], Jian-zheng WU[5], Shao-kang GUAN[1]

1. School of Materials Science and Engineering, Zhengzhou University, Zhengzhou 450001, China;
2. Guizhou Aerospace Xinli Technology Co., Ltd., Guizhou 563000, China;
3. Manufacturing Center, CRRC Times Electric Co., Ltd., Zhuzhou 412001, China;
4. Key Laboratory of Material Physics, Ministry of Education,
School of Physics and Microelectronics, Zhengzhou University, Zhengzhou 450052, China;
5. Key Laboratory of Precious Metals Analysis and Exploration Technology of Ministry of Natural Resources,
Zhengzhou 450012, China

Received 5 April 2022; accepted 21 September 2022

Abstract: The wide crystallization temperature range of Al−Mg alloys is a key factor for the surface defect formation during continuous casting and rolling process. To reduce the crystallization temperature range of the alloy, the influences of trace Zn, Si, Zr and Ti elements on the microstructure and properties of Al−2Mg−0.5Mn alloy were investigated. The X-ray photoelectron spectroscopy, atomic force microscopy, scanning and transmission electron microscopy were used for microstructural characterization. The Ti and Zr additions could refine the grain size and improve the strength of the Al−Mg−Mn alloy by forming Al_3Ti and Al_3Zr in the alloy, while the crystallization temperature ranges of these alloys were wider. It was revealed that Zn and Si additions could form new secondary phases with Mg in the alloy, thus reducing the actual Mg content during later eutectic solidification process. Therefore, the crystallization temperature range of Al−2Mg−0.5Mn−0.2Zn−0.2Si alloy was narrower than that of Al−2Mg−0.5Mn alloy. The mechanical properties and corrosion resistance of Al−2Mg−0.5Mn alloy were also improved by the additions of Zn and Si.

Key words: Al−Mg alloy; continuous casting and rolling; mechanical properties; corrosion behavior; crystallization temperature range

1 Introduction

Al−Mg (5xxx) alloys have been extensively employed in the transportation, construction and aerospace industries, owing to their high specific strength, low density, and excellent corrosion resistance [1−3].

Currently, the hot rolling, twin-roll casting, and continuous casting and rolling process (CCRP) are commonly used to produce aluminum alloy sheets [4,5]. The manufacturing performance and surface quality of the sheet produced by hot rolling and twin-roll casting process are excellent. However, these products are very expensive due to the high cost of the production line, complicated processing technology, long production cycle and high energy consumption.

The ingot milling and heating processes are not necessary for CCRP. The layout of the production line is simple, which can significantly reduce the production process. It has the advantages of high production and high efficiency, low energy consumption and low costs [6]. However, the CCRP

Corresponding author: Yun-jia SHI, Tel: +86-371-67783170, E-mail: yunjiashi@zzu.edu.cn
DOI: 10.1016/S1003-6326(23)66306-X

can only be used for 3xxx series aluminum alloys or pure aluminum at present. For the Al−Mg alloys, surface defects are prone to be formed during the process, because the crystallization temperature range of alloy is too wide.

The crystallization temperature range of Al−3Mg−0.5Mn alloy was reported to be 22.5 °C [7]. The cooling rate in CCRP was very large, so the duration time of the solid and liquid two-phase region was further extended due to the high degree of supercooling. As a result, the surface morphology of the rolled plate was poor and the metallurgical defects such as pores and inclusions were observed in the final product. Unfortunately, it is difficult to improve the quality of ingots and final products through technical routes. Therefore, there is an urgent need to develop new 5xxx series aluminum alloys that can be produced by CCRP with high quality.

Magnesium is the major alloying element in Al−Mg (5xxx) alloys [8,9], which can produce solid solution strengthening effect. However, the β phase (Al_3Mg_2) can be formed in Al−Mg alloys when the content of Mg is high, leading to higher intergranular corrosion and stress corrosion sensitivity [10,11]. The strength of Al−Mg alloys was relatively lower than that of the age hardening aluminum alloys [12−14]. For such non-heat treatable aluminum alloys, work hardening and microalloying were often used to increase their strength [15]. For instance, $TiAl_3$ particles can be formed in Al alloys after the addition of Ti [16,17], and the grain size can be refined due to the inhomogeneous nucleation during crystallization process. The addition of Mn contributes to the uniform distribution of precipitates in Al alloys, which can also hinder the recrystallization process and improve the strength and stability of the alloy [18]. Al_3Zr compounds can be formed with Al after the addition of Zr, which can also refine the grains of the as-cast alloy, hinder the recrystallization process, and enhance the crack initiation resistance of the alloy [19−21].

However, the crystallization temperature range of the alloy generally increases with the additions of alloying elements. Therefore, alloying elements that can form compounds with the main alloying element Mg in the alloy, such as Si and Zn [17,22], should also be researched. It can reduce the magnesium content for eutectic reaction with the aluminum matrix during casting. The crystallization temperature range of the alloy decreases with the decreasing of eutectic reaction time.

The aim of the current work is to decrease the crystallization temperature range and improve the properties of Al−Mg alloy by adding trace elements. The effects of Zn, Si, Zr and Ti on the crystallization temperature range, microstructure, mechanical properties, and corrosion properties of Al−2Mg−0.5Mn alloy were studied.

2 Experimental

2.1 Materials

The CCRP cannot be realized in the lab now. Since it needs a great deal of Al alloy (10 t or more) in the factory, the traditional melting and casting were carried out in the lab. The Al−2Mg−0.5Mn, Al−2Mg−0.5Mn−0.2Zn−0.2Si, Al−2Mg−0.5Mn−0.2Zn−0.2Zr, Al−2Mg−0.5Mn−0.2Zn−0.2Ti, Al−2Mg−0.5Mn−0.2Si−0.2Zr and Al−2Mg−0.5Mn−0.2Si−0.2Ti researched in this study were named $1^{\#}$−$6^{\#}$, respectively. The alloys melts were poured into a 100 mm × 100 mm × 8 mm steel mold. The ingots were homogenized at 460 °C for 24 h. To research the mechanical properties and corrosion resistance of different alloys, the ingots were cold-rolled into 2 mm-thick plates.

2.2 Microstructure characterization

Microstructure characterization was performed using an Auriga (Zeiss, 30 kV) FIB scanning electron microscope (SEM) equipped with an energy dispersive spectroscopy (EDS) and electron backscatter diffraction (EBSD) system, and transmission electron microscopy (TEM) images were obtained by FEI Talos F200S (FEI, 200 kV) equipped with EDS. SEM and EBSD samples were prepared by electropolishing with a solution of 90% absolute C_2H_5OH and 10% $HClO_4$. The starting voltage was 25−60 V, and the electrolysis time was 6−35 s. The Leica EMRES 102 ion beam polishing system was used for surface polishing. Channel 5 software was used to analyze the EBSD data. TEM samples were prepared by twin-jet electropolishing in 75% methanol and 25% HNO_3 (volume fraction) solution at approximately −20 °C.

The corrosion products after electrochemical

corrosion were determined by Axis Supra X-ray photoelectron spectroscopy (XPS, Axis Supra) with Al K_α. The vacuum during the test was controlled within 6.65×10^{-7} Pa, and the binding energies of the tested curves were calibrated with C 1s= 284.8 eV.

The STA 449F3 (German Netzsch) calorimeter was used for thermal analysis and testing of the line-difference (differential) scanning calorimeter (DSC). The temperature range was 25−800 °C, and the heating and cooling rate was 10 °C/min. According to the DSC curves of the alloy, the solidus temperature of the alloy was the temperature corresponding to the initial location of the homoeothermic peak during melting, and the liquidus temperature of the alloy is the temperature corresponding to the initial location of the exothermic peak during solidification [23]. The difference between the solidus temperature and the liquidus temperature was regarded as the crystallization temperature range of the alloy.

According to GB/T 16865—2013, the rolled plate was machined along the rolling direction into a dog bone shape tensile specimens with a gauge length of 25 mm and width of 6 mm. Then, the burrs were polished off from the specimens with sandpaper and the tensile tests were carried out at a tensile rate of 2 mm/min. Three specimens of each alloy were prepared and the mean value was used as the test result.

The electrochemical test was carried out on an RST5200F (RST Electrochemical Workstation) using a three-electrode working system. The sample was used as the working electrode, the reference electrode was a saturated calomel electrode, and the auxiliary electrode was a platinum electrode. The test was carried out in 3.5 wt.% sodium chloride solution, and the scanning speed was 0.5 mV/s.

The degree of intergranular corrosion resistance was estimated by the nitric acid mass loss test (NAMLT). The experiment mainly referred to ASTM G67—2013 [24].

The Kelvin probe force microscopy mode of atomic force microscopy (AIST-NT, AFM) was used to explore the potential between the secondary phase and the Al matrix of the polished cold-rolled plate surface on an area of 100 μm × 100 μm. LabRAM HR Evo's AIST-NT atomic force microscope and software were used.

3 Results

3.1 DSC analysis of as-cast alloys

DSC was used to determine the crystallization temperature range of the alloy. The DSC curves of the as-cast alloys are shown in Fig. 1. An obvious exothermic peak during the cooling process and an obvious endothermic peak during the heating process could be observed on the DSC curves of each alloy.

According to the DSC curves of the as-cast alloys with different composition in Fig. 1, the liquidus temperature (LT), solidus temperature (ST), and crystallization temperature range corresponding to different compositions are given in Table 1.

It is revealed that the narrowest crystallization temperature range among these alloys is Al−2Mg−0.5Mn−0.2Zn−0.2Si, in which the crystallization temperature range falls below 5 °C. The crystallization temperature range of Al−2Mg−0.5Mn−0.2Zn−0.2Si was about 80% smaller than that of the Al−3Mg−0.5Mn alloy [7].

3.2 Microstructure of cold-rolled alloys

The backscattered SEM micrographs of the cold-rolled alloys and the distribution of the main elements are shown in Fig. 2. There were mainly two types of phases in the Al−2Mg−0.5Mn−0.2Zn−0.2Si alloy, as shown in Fig. 2(a). The white intermetallic compounds were intermittent, while the gray compounds were more continuous. The mapping images show that the white particles are mainly the Al_6Mn phases [25−27] and the gray areas are mainly the Mg_2Si phases. Figure 2(b) shows the backscattered SEM image and EDS main element distribution obtained in rolled Al−2Mg−0.5Mn−0.2Si−0.2Zr alloy, which was confirmed the existence of two kinds of particles.

The element distribution maps of Al, Mn, Mg, Si, and Zr indicated that the white phase mainly include Al and Mn, while the black phase include Mg and Si, and the distribution of Zr was more dispersed. Therefore, the white particles were mainly Al_6Mn phase, and the black particles were Mg_2Si phase [28]. The backscattered SEM image and main element distribution of cold-rolled Al−2Mg−0.5Mn−0.2Si−0.2Ti are displayed in Fig. 2(c). The gray secondary particles were Mg_2Si

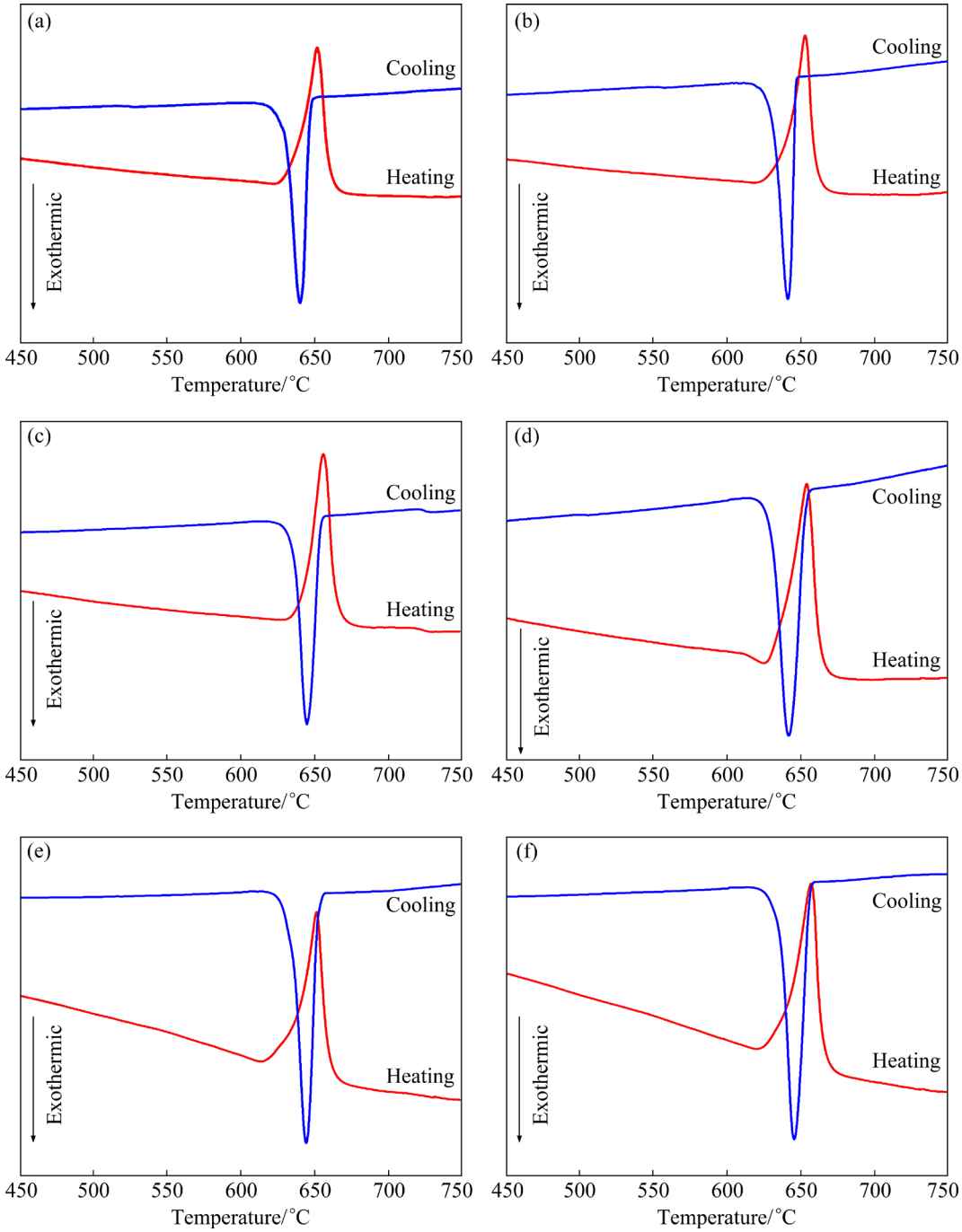

Fig. 1 DSC curves of as-cast alloys: (a) 1#; (b) 2#; (c) 3#; (d) 4#; (e) 5#; (f) 6#

Table 1 Crystallization temperature range of as-cast alloys

Alloy	Liquidus temperature/°C	Solidus temperature/°C	Range/ °C
1#	646.5	638.3	8.2
2#	646.4	641.8	4.6
3#	653.6	643.4	10.2
4#	652.7	639.5	13.2
5#	651.6	640.9	10.7
6#	655.2	642.5	12.7

phase, and the white particles were Al_6Mn phases. In addition, there were some Ti-containing particles.

Typical TEM images of the cold-rolled alloys are shown in Fig. 3. A large number of dislocations and high-density dislocation tangles could be observed in the cold-rolled alloy [29]. Grain boundaries could not be discovered due to residual stress generated by cold rolling, and only fuzzy grain boundaries and dislocation tangles composed

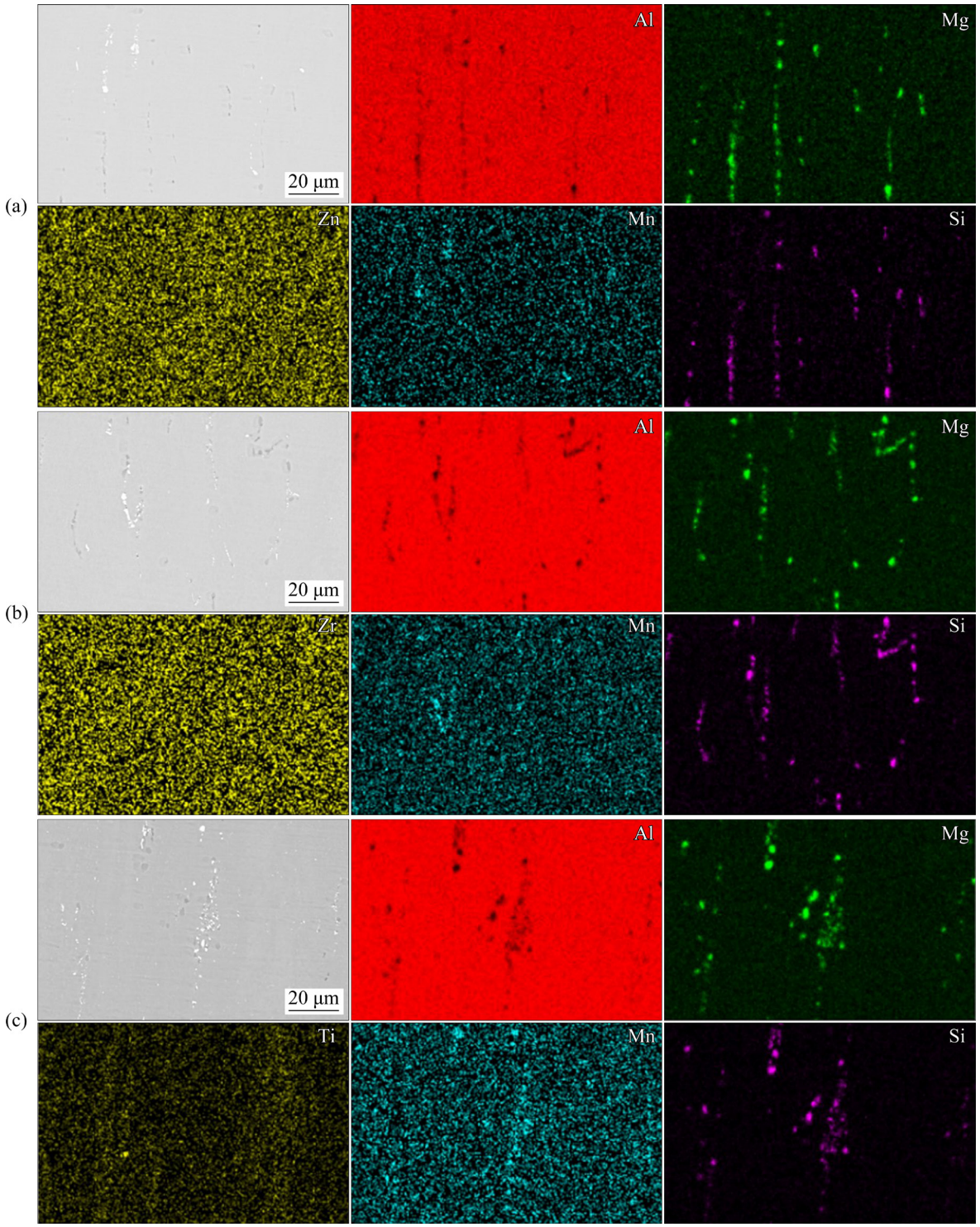

Fig. 2 Backscattered electronic images and elements distribution of cold-rolled alloys: (a) 2#; (b) 5#; (c) 6#

of dense dislocations could be observed. In addition, the observed streaks were recognized as a corrugated pattern, which is often discovered in cold-rolled alloys [30]. There were mainly two kinds of grain boundaries in the strip-like structure. One was the grain boundary parallel or approximately parallel to the rolling direction, which is called the geometrically necessary boundary (GNB). The other was the grain boundary between and perpendicular to the strips, called the incidental dislocation boundary (IDB), which was mainly low-angle grain boundary. The internal dislocation density and dislocation tangles significantly increased after adding trace alloying

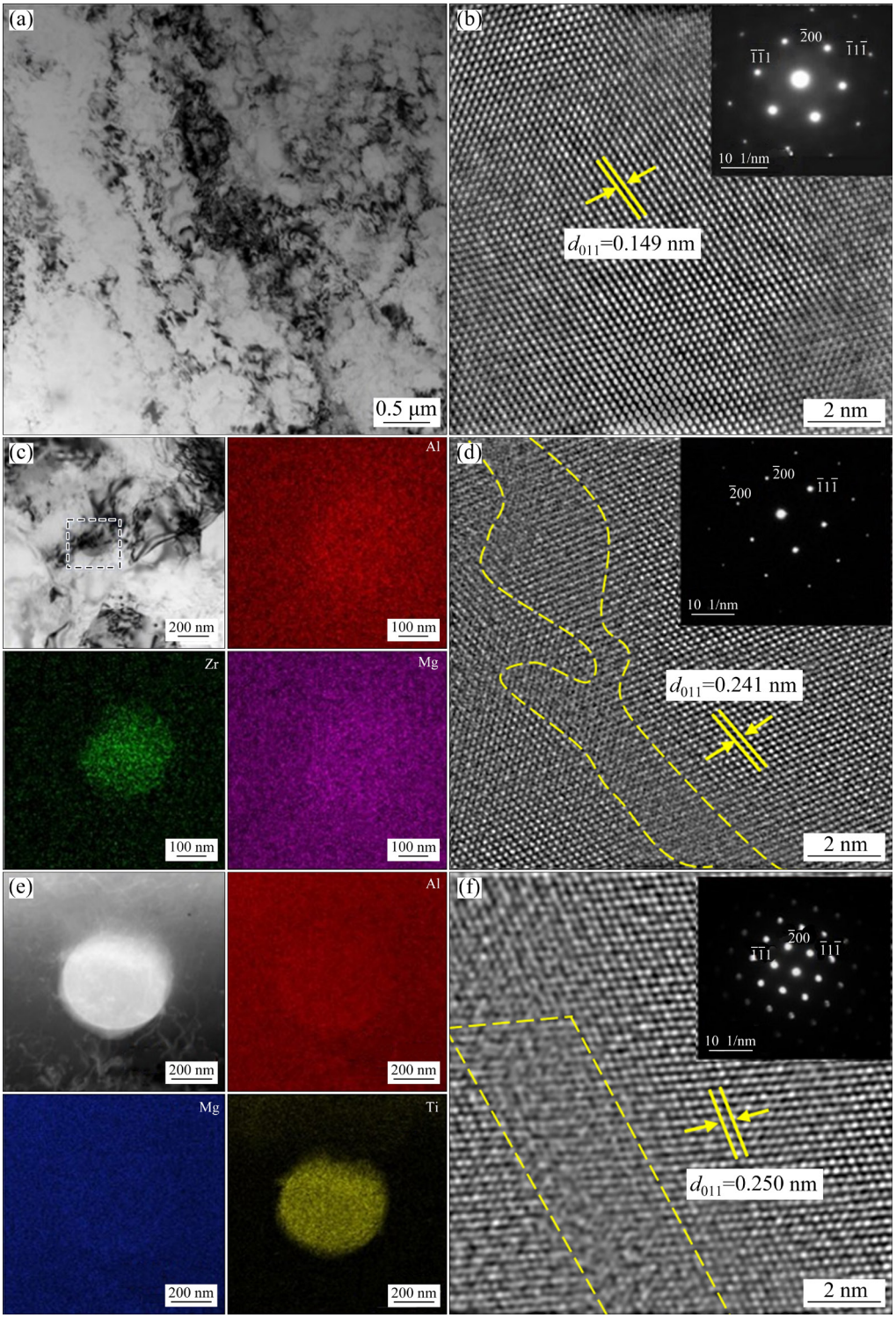

Fig. 3 TEM images of rolled alloys: (a, b) Bright-field image and HRTEM image of 1# alloy; (c, d) Main element distributions and HRTEM image of 3# alloy; (e, f) Main element distributions and HRTEM image of 4# alloy

elements to the Al−2Mg−0.5Mn alloy. The main element distribution of Al−2Mg−0.5Mn−0.2Zn−0.2Zr (3#) alloy and Al−2Mg−0.5Mn−0.2Zn−0.2Ti alloy (4#) are shown in Figs. 3(c) and (e), respectively. The secondary phase precipitated on the grain boundary with a large number of dislocations around them. As shown in Fig. 3(e), the spherical secondary phase in 3# alloy mainly contained Al and Zr, and the spherical secondary phase in the Al−2Mg−0.5Mn−0.2Zn−0.2Ti alloy (4#) mainly contained Al and Ti, which could be identified as the Al_3Ti phases. The high-resolution

transmission electron microscopy (HRTEM) images of 1#, 3# and 4# alloys are shown in Figs. 3(b, d, f), respectively. A large number of lattice distortion regions could be observed in different cold-rolled alloys [31,32]. After adding elements to the Al−2Mg−0.5Mn alloy, the lattice distortion in the alloy became more serious. Dislocation accumulation was found in these areas (yellow circled area), which can provide the driving force for dynamic recrystallization [33]. It could also be found that the additions of trace elements to the alloy can increase the lattice constant and interatomic distance of the Al−2Mg−0.5Mn alloy.

The grain orientation distribution maps of the cold-rolled Al−2Mg−0.5Mn-based alloys is shown in Fig. 4. LAGBs and HAGBs are represented by black and gray lines, respectively. After 77% cold rolling deformation of alloys, the original equiaxed grains of the alloys were elongated along the rolling direction, showing typical fibrous structure. The grains of Al−2Mg−0.5Mn alloys were refined after adding alloy elements. In particular, the grains in alloys with Ti and Zn, Ti and Si were smaller and straighter than those in other alloys. The addition of Ti can form Al_3Ti phase with the Al matrix, which can act as heterogeneous nucleation sites during crystallization and refine the microstructure of the alloy. In Figs. 4(a−c), different degrees of texture at 30°−45° to the rolling direction were observed.

The orientation maps of the samples are shown in Fig. 5. All textures distributed along the rolling direction. The percentage of typical textures is given in Table 2. It can be observed that the proportion of Brass texture is the highest in the

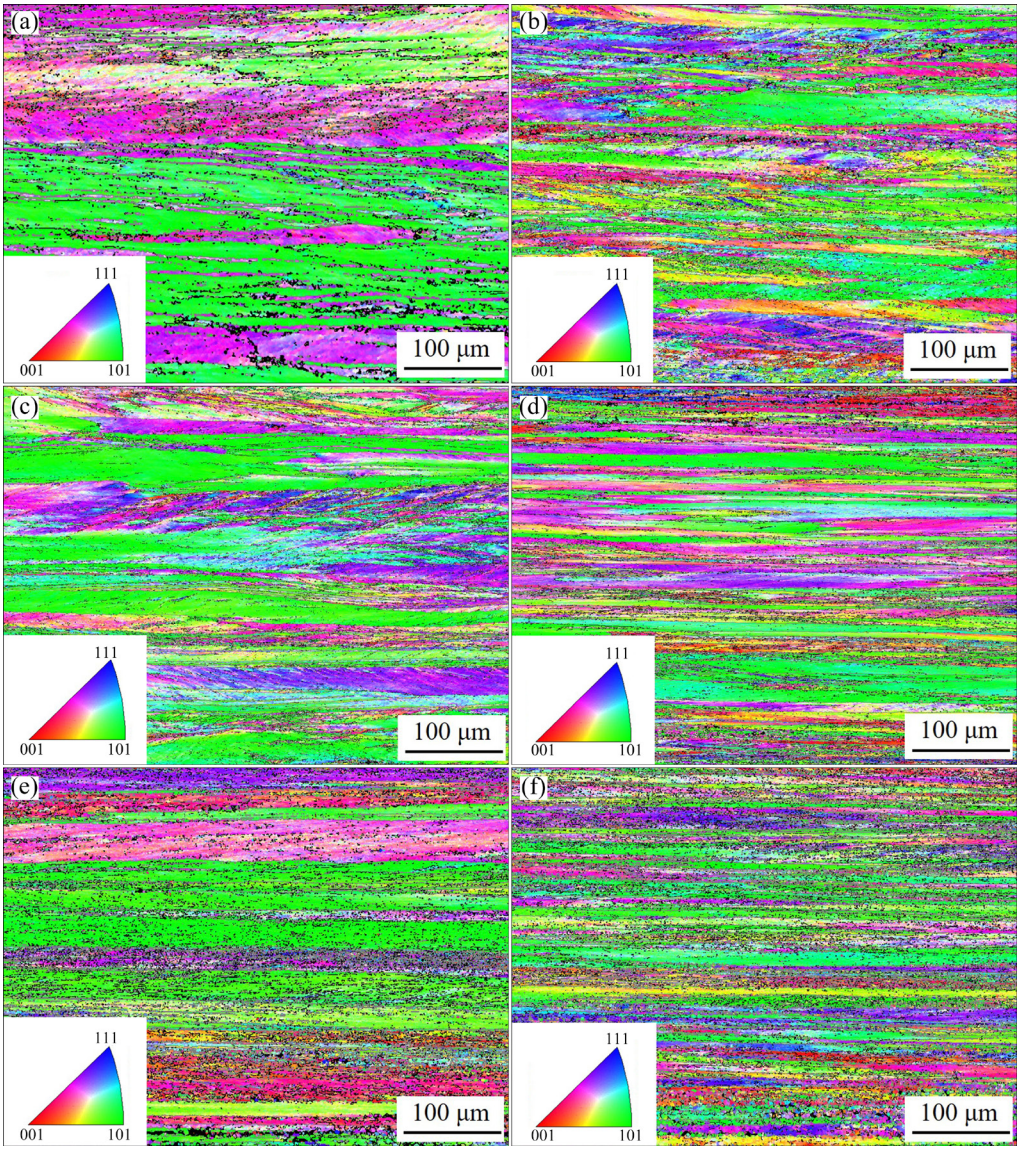

Fig. 4 EBSD images of cold-rolled alloys: (a) 1#; (b) 2#; (c) 3#; (d) 4#; (e) 5#; (f) 6#

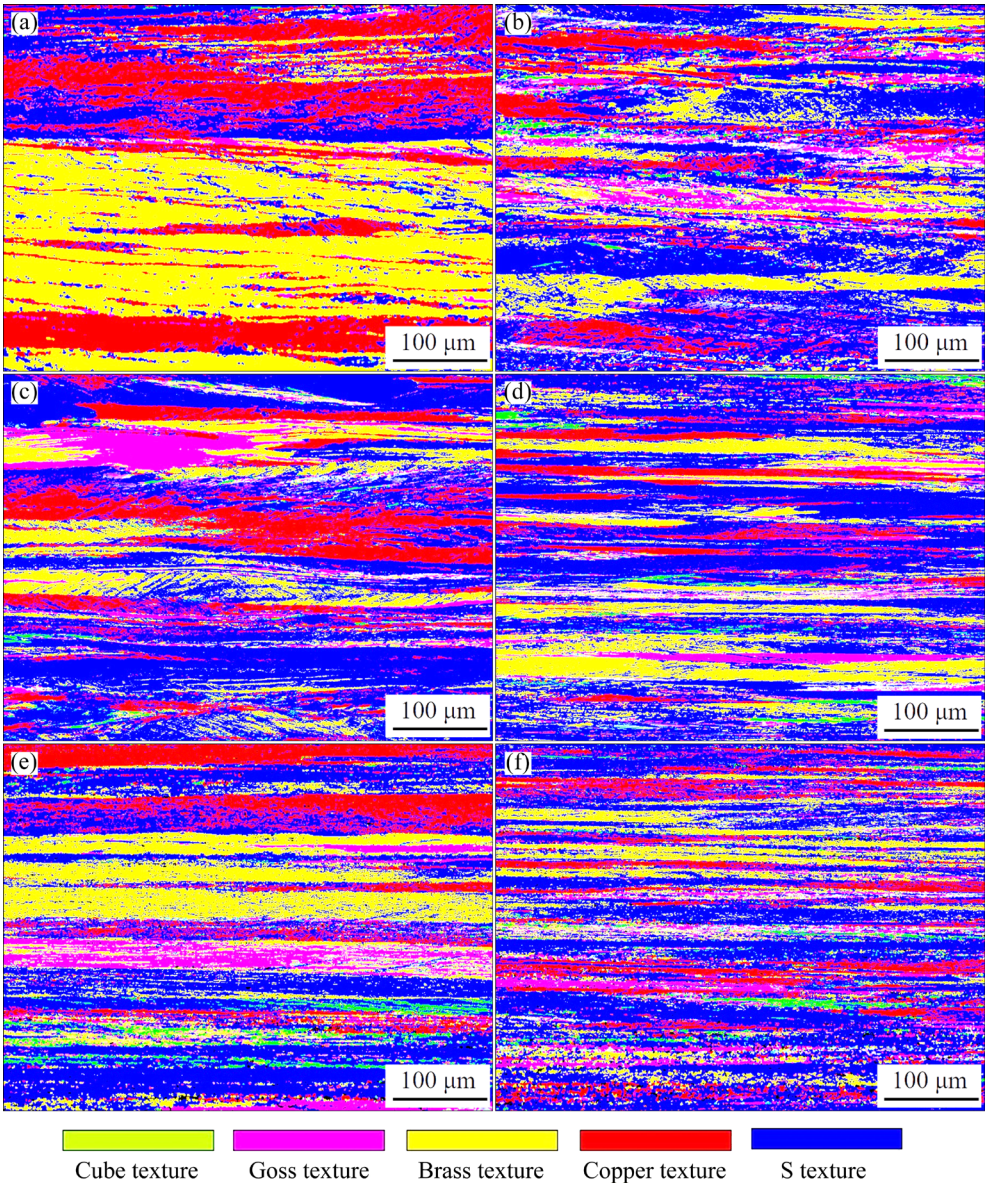

Fig. 5 Orientation maps of cold-rolled alloys: (a) 1#; (b) 2#; (c) 3#; (d) 4#; (e) 5#; (f) 6#

Table 2 Percentage of textures in cold-rolled alloys (%)

Sample	S texture	Copper texture	Brass texture	Goss texture	Cube texture	Other textures
Al−2.0Mg−0.5Mn	24.0	33.1	40.1	1.5	0.1	1.2
Al−2.0Mg−0.5Mn−0.2Zn−0.2Si	52.8	13.3	15.9	5.6	1.4	11.1
Al−2.0Mg−0.5Mn−0.2Zn−0.2Zr	54.7	19.1	14.4	6.5	0.9	4.5
Al−2.0Mg−0.5Mn−0.2Zn−0.2Ti	55.0	9.11	19.2	4.1	2.2	10.5
Al−2.0Mg−0.5Mn−0.2Si−0.2Zr	44.4	15.3	20.4	8.0	3.4	8.5
Al−2.0Mg−0.5Mn−0.2Si−0.2Ti	53.4	14.0	13.3	4.9	2.1	12.3

Al−2Mg−0.5Mn alloy, followed by Copper texture and S texture. However, the ratio among these three textures changed significantly after adding trace alloying elements to Al−2Mg−0.5Mn alloy. The content of S texture increased fast, while the Brass texture and Copper texture both decreased. This shows that the alloy composition would affect the texture of the alloy.

3.3 Mechanical properties

To understand the influence of different alloying elements on the mechanical properties of Al−2Mg−0.5Mn alloy, tensile tests and hardness tests were conducted. The yield strength (YS), ultimate tensile strength (UTS), and elongation (El) of different alloys are summarized in Table 3. It can be observed that adding trace amounts of alloying elements to the Al−2Mg−0.5Mn alloy can improve the tensile strength slightly. This may be related to the presence of different secondary phases in these alloys, such as Al_3Zr, Al_3Ti, $MgZn_2$ and Mg_2Si. These phases can all increase the strength of the alloys. Higher contents of S texture can be observed after adding different elements, which could also influence the strength of the alloy. Among the cold-rolled alloys in this experiment, the tensile strength of Al−2Mg−0.5Mn−0.2Si−0.2Ti alloy is the highest, followed by the Al−2Mg−0.5Mn−0.2Zn−0.2Ti alloy.

Table 3 Mechanical properties of alloys

Alloy	YS/MPa	UTS/MPa	El/%
Al−2Mg−0.5Mn	212.5	256.0	3.4
Al−Mg−Mn−0.2Zn−0.2Si	196.3	262.0	2.7
Al−Mg−Mn−0.2Zn−0.2Zr	221.3	266.8	2.7
Al−Mg−Mn−0.2Zn−0.2Ti	230.7	274.7	4.4
Al−Mg−Mn−0.2Si−0.2Zr	208.5	270.3	2.3
Al−Mg−Mn−0.2Si−0.2Ti	222.6	282.6	4.0

3.4 Corrosion behaviors

The intergranular corrosion sensitivity of the alloys was tested by NAMLT, and the results are shown in Fig. 6. The degree of sensitization value of all test alloys was less than 3.5 mg/cm^2. The material with a mass loss of less than 15 mg/cm^2 could be judged to be resistant to intergranular materials according to the ASTM G67 standard, so these alloys were all intergranular corrosion resistant materials. It was not easy for the β phase to precipitate at the grain boundaries due to the relatively low Mg content. Moreover, it can be concluded that these secondary phase particles formed by the additions of different alloying elements did not affect the corrosion resistance of the alloy [34,35].

The polarization curves of the cold-rolled experimental samples were tested in 3.5 wt.% NaCl solution at room temperature, and the results are shown in Fig. 7. The polarization curve in the anode region of the Al−2Mg−0.5Mn−0.2Si−0.2Ti alloy showed induced pitting corrosion followed by active corrosion, in which no passive platform was observed. However, the polarization curves of other alloys showed spontaneous passivation before being significantly broken down by pitting corrosion. Table 4 presents the values of the corrosion potential (φ_{corr}) and the corrosion current density (J_{corr}) resulted from the Tafel curves in Fig. 7. The φ_{corr} of the Al−2Mg−0.5Mn−0.2Si−0.2Zr alloy was more positive than that of the other alloys, and the corrosion current density of the Al−2Mg−0.5Mn−0.2Zn−0.2Zr alloy was significantly lower than that of the Al−2Mg−0.5Mn alloy. It can also be observed that the φ_{corr} values increased and the J_{corr} values decreased, showing higher corrosion resistance of Al−2Mg−0.5Mn alloys after adding different alloying elements.

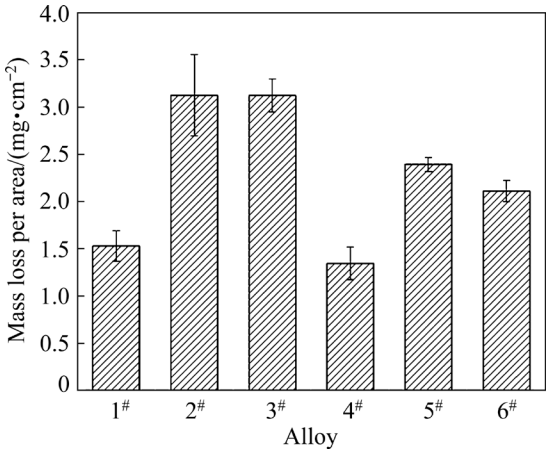

Fig. 6 Nitric acid mass loss test (NAMLT) result of cold-rolled alloy

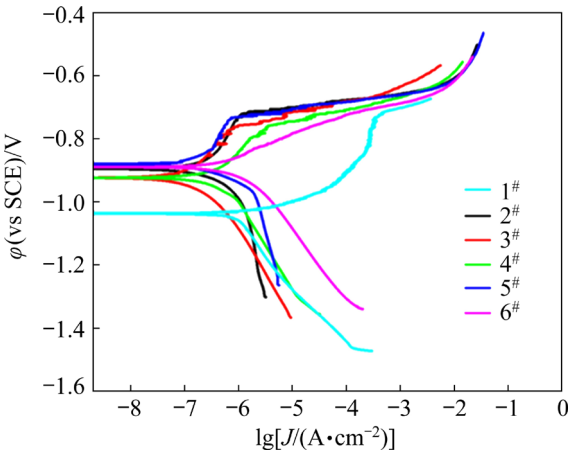

Fig. 7 Polarization curves of cold-rolled alloys

Table 4 Electrochemical parameters of cold-rolled alloys

Alloy	φ_{corr}(vs SCE)/V	J_{corr}/(A·cm^{-2})
1#	−1.038	7.606×10^{-7}
2#	−0.896	1.146×10^{-7}
3#	−0.924	5.175×10^{-8}
4#	−0.924	1.705×10^{-7}
5#	−0.881	1.098×10^{-7}
6#	−0.890	3.590×10^{-7}

The electrochemical corrosion products of the experimental alloys were investigated by XPS. Since compact oxide film can be formed on the surface of aluminum alloys, it can prevent the alloy from being further oxidized [36] and therefore presents excellent corrosion resistance. To reveal the proportion of corrosion products and remaining oxide film on the surface after the electrochemical reaction, the Al 2p and O 1s spectra of the alloy were fitted, as shown in Fig. 8. After the electrochemical corrosion, the surface Al elements of the experimental alloy were mainly in the formation of Al, Al_xO_y, and $Al(OH)_3$ [37,38]. The corresponding binding energies were 72.8, 75.5, and 74.4 eV, respectively. The O elements were mainly in the form of H_2O, Al_2O_3, and $Al(OH)_3$ [39]. The corresponding binding energies were 534.0, 532.9 and 531.9 eV, respectively. This is in the initial stage of electrochemical corrosion, where Al^{3+} reacted with OH^- to form $Al(OH)_3$. As the reaction progresses, unstable $Al(OH)_3$ could be quickly dehydrated into Al_2O_3 and H_2O. Therefore, the surface of the cold-rolled alloy sample was mainly composed of the passive film Al_2O_3 and the corrosion product $Al(OH)_3$ after electrochemical corrosion in a 3.5 wt.% NaCl solution [40].

4 Discussion

The crystallization temperature range of Al−2Mg−0.5Mn-based alloys was obviously smaller than that of Al−3Mg−0.5Mn alloy, indicating that the crystallization temperature range of Al−Mg alloy was mainly affected by Mg content. To research the influence of Mg content in Al−Mg alloys, the Al−Mg binary phase diagram is drawn by Pandat® software, as shown in Fig. 9.

The liquidus temperature and the solidus temperature of Composition C_1 were T_1 and T_1', respectively, and those of C_2 were T_2 and T_2', respectively. It can be seen from the phase diagram that the temperature difference between the solid–liquid lines of C_1 is significantly smaller than that of C_2. Therefore, when the magnesium content is lower than 10 wt.%, crystallization temperature range increases with the Mg content, which is mainly due to the fact that the eutectic reaction time of Al and Mg increases. The additions of Zn and Si to the Al−2Mg−0.5Mn alloy effectively reduced its crystallization temperature range, as shown in Fig. 1. This is mainly due to the fact that the addition of Zn can form the MgZn mesophase with Mg in the alloy, such as $MgZn_2$ and $Mg_{32}(Al,Zn)_{49}$, which can consume some Mg atoms in alloy [7]. Moreover, Mg_2Si phase can be formed in the alloy with the addition of Si, which also consumes some Mg atoms and reduces the Mg content for the eutectic reaction in the alloy. Therefore, the crystallization temperature range of the alloy was significantly reduced by Zn and Si additions to the Al−2Mg−0.5Mn alloy. However, with the additions of other elements, the crystallization temperature range of the alloy was slightly larger than that of Al−2Mg−0.5Mn. This is due to the fact that Al_3Zr dispersed phase can be formed after the addition of Zr, and Al_3Ti phase can be formed after the addition of Ti, as shown in Fig. 3. The additions of both Zr and Ti consumed a certain amount of Al, which can increase the relative ratio of Mg/Al in the alloy. Additionally, more types and contents of alloying elements can lead to the higher crystallization temperature and cause more complex reactions to be finished during the crystallization process, so the crystallization temperature range increases slightly after adding Ti and Zr.

AFM was used to explore the potential between secondary phase and Al matrix of the polished cold-rolled sheet surface, and the results are shown in Fig. 10. The secondary phase (bright area) and the aluminum matrix (dark area) can be clearly separated in the potential diagram, but the types of different phases cannot be clearly distinguished. Compared with the Al−2Mg−0.5Mn alloy, alloys with additions of different elements presented a smaller potential difference with the matrix. Since the secondary phases of Mg_2Si, $MgZn_2$, Al_3Zr or Al_3Ti in Al−Mg−Mn alloys with the additions of Zn, Si, Zr and Ti cannot form a large potential difference with the aluminum matrix

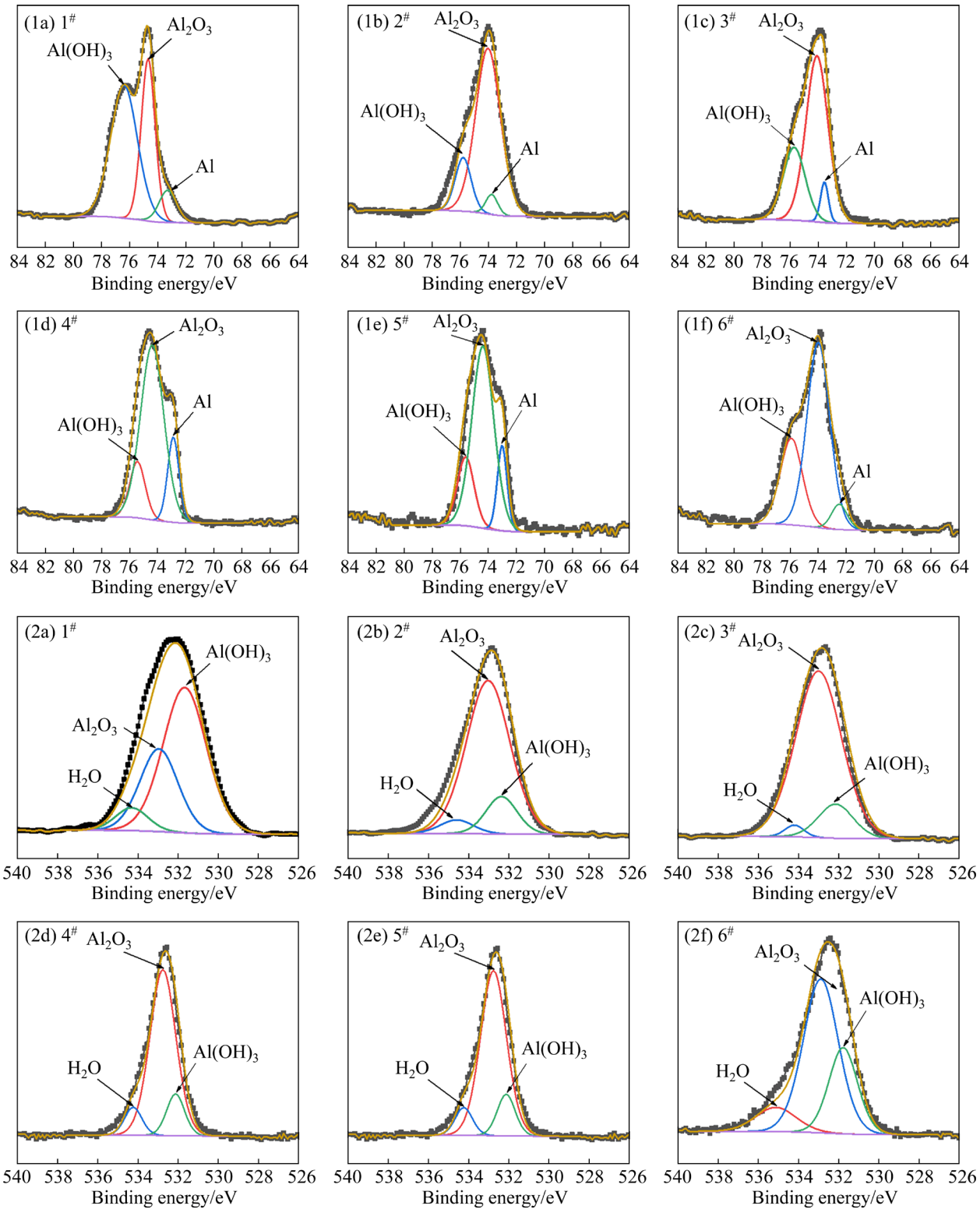

Fig. 8 XPS spectra fitting after electrochemical corrosion of cold-rolled alloy: (1a−1f) High-resolution spectra of Al 2p ($1^{\#}$−$6^{\#}$); (2a−2f) High-resolution spectra of O 1s ($1^{\#}$−$6^{\#}$)

and the amount of these secondary particles was small, no obvious corrosion sensitivity of Al−Mg−Mn alloys increased after adding trace elements.

Adding Ti to Al−2Mg−0.5Mn could increase the strength of the alloy more than other alloying elements. This is mainly because Ti can refine the as-cast grains and greatly improve mechanical

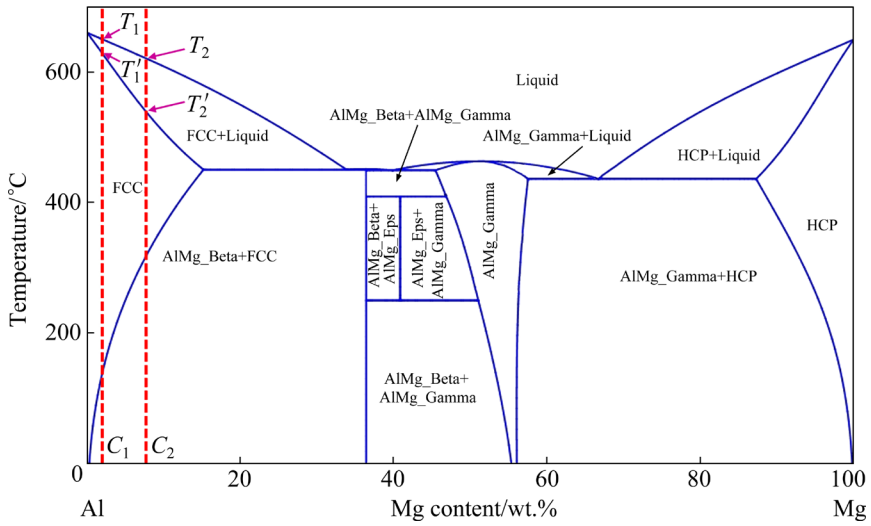

Fig. 9 Al−Mg binary phase diagram obtained by Pandat® software

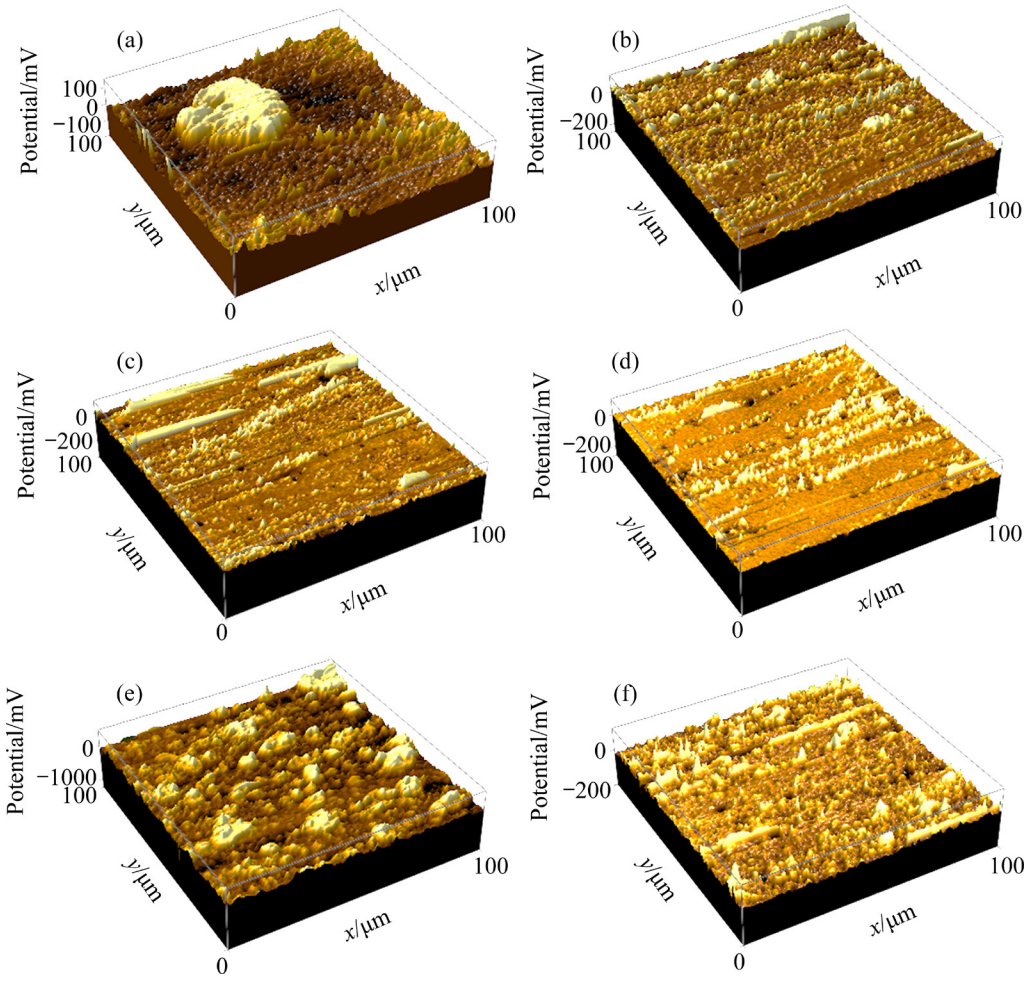

Fig. 10 Potential distribution of cold-rolled alloys obtained by AFM: (a) 1#; (b) 2#; (c) 3#; (d) 4#; (e) 5#; (f) 6#

performance after the subsequent heat treatment and rolling process of the Al−Mg alloy. The effects of other elements on the strength of the three alloys were not so obvious. In 5xxx aluminum alloys, strain hardening and solid solution strengthening of magnesium are the main strengthening mechanisms of aluminum−magnesium alloys. Microalloying is an important method to further increase the strength

of alloys. However, solution and aging treatments are needed to precipitate large amounts of secondary phases after adding elements. For example, after being solution-treated at about 500 °C, a high volume fraction of $MgZn_2$ particles needs to be artificially aged at 100−170 °C [41,42], Mg_2Si particles at 120−200 °C [43], and Al_3Zr particles at approximately 370 °C [44]. However, the dislocation density of the alloys will decrease obviously after solution treatment, which can decrease the effect of strain hardening. Therefore, no solution and aging were researched about these alloys. As a result, the improvements of strength in the as-cold rolled Al−Mg−Mn alloys with the additions of Si, Zn and Zr were not so obvious.

In general, the mechanical properties and corrosion resistance of Al−Mg−Mn alloys were both increased by adding alloying elements, while Al−2Mg−0.5Mn−0.2Zn−0.2Si was the only alloy with crystallization temperature range lower than that of Al−2Mg−0.5Mn alloy. It is the most promising alloy that could be used for continuous casting and rolling processes. The next step of our work is to produce and research the microstructure and properties of Al−2Mg−0.5Mn−0.2Zn−0.2Si alloy using CCRP in the factory.

5 Conclusions

(1) The additions of Zn and Si to the Al−2Mg−0.5Mn alloy decreased the crystallization temperature range and the crystallization temperature range of the Al−2Mg−0.5Mn−0.2Zn−0.2Si alloy was 4.6 °C. However, the additions of Zr and Ti increased the crystallization temperature range of the alloy.

(2) The percentage of brass texture was the highest in Al−2Mg−0.5Mn alloy. After adding other elements, the proportion of S texture increased.

(3) The tensile strength and hardness of the Al−2Mg−0.5Mn alloy were improved by adding trace elements. Among them, the strength of the Al−2Mg−0.5Mn−Si−Ti alloy was the highest, mainly owing to the smaller grain size.

(4) The NAMLT results of all the studied alloys were ranged from 1.34 to 3.13 mg/cm^2, which were all less than 15 mg/cm^2. The additions of Zn, Si, Zr and Ti can improve the corrosion resistance of Al−Mg−Mn alloys.

(5) Al−2Mg−0.5Mn−0.2Zn−0.2Si was found to be the most promising alloy for continuous casting and rolling processes.

Acknowledgments

This work was supported by the National Natural Science Foundation of China (No. 51901207).

References

[1] MA Ru-long, PENG Chao-qun, CAI Zhi-yong, WANG Ri-chu, ZHOU Zhao-hui, LI Xiao-geng, CAO Xuan-yang. Finite element analysis of temperature and stress fields during selective laser melting process of Al−Mg−Sc−Zr alloy [J]. Transactions of Nonferrous Metals Society of China, 2021, 31(10): 2922−2938.

[2] LEI Chuan, WANG Qu-dong, TANG Hua-ping, LIU Tian-wen, LI Zhong-yang, JIANG Hai-yan, WANG Kui, DING Wen-jiang. Effects of Mg content on microstructure and mechanical properties of low Zn-containing Al−*x*Mg−3Zn−1Cu cast alloys [J]. Transactions of Nonferrous Metals Society of China, 2022, 32(3): 721−738.

[3] RADOVIĆ L J, NIKAČEVIĆ M, JORDOVIĆ B. Deformation behaviour and microstructure evolution of AlMg6Mn alloy during shear spinning [J]. Transactions of Nonferrous Metals Society of China, 2012, 22(5): 991−1000.

[4] XU Mian-guang, LI Zhong-yang, WANG Zhao-hui, ZHU Miao-yong. Computational and experimental study of the transient transport phenomena in a full-scale twin-roll continuous casting machine [J]. Metallurgical and Materials Transactions B, 2017, 48: 471−487.

[5] XU Mian-guang, ZHU Miao-yong. Numerical simulation of the fluid flow, heat transfer, and solidification during the twin-roll continuous casting of steel and aluminum [J]. Metallurgical and Materials Transactions B, 2016, 47: 740−748.

[6] AMIRI M M, FERESHTEH F. An experimental investigation on the effect of cooling rate during combined continuous casting and rolling process on mechanical properties of 7075 aluminum alloy [J]. Transactions of the Indian Institute of Metals, 2020, 73(2): 441−448.

[7] LI Qian-qian, LI Meng-jia, LU Guang-xi, GUAN Shao-kang, ZHANG En-gui, XU Cong. Effect of trace elements on the crystallization temperature range and properties of 5xxx series aluminum alloys [J]. Metals, 2020, 10(4): 483−499.

[8] CAO Fu-rong, YIN Bin, LIU Si-yuan, SHI Lu, WANG Shun-cheng, WEN Jing-lin. Microstructural evolution, flow stress and constitutive modeling of Al−1.88Mg−0.18Sc−0.084Er alloy during hot compression [J]. Transactions of Nonferrous Metals Society of China, 2021, 31(1): 53−73.

[9] VYSOTSKIY I, KIM K, MALOPHEYEV S, MIRONOV S, KAIBYSHEV R. Superplastic behavior of friction-stir welded Al−Mg−Sc−Zr alloy in ultrafine-grained condition [J]. Transactions of Nonferrous Metals Society of China, 2022, 32(4): 1083−1095.

[10] YI Gao-song, CULLEN D A, LITTRELL K C, GOLUMBFSKIE W, SUNDBERG E, FREE M L.

Characterization of Al−Mg alloy aged at low temperatures [J]. Metallurgical and Materials Transactions A, 2017, 48(4): 2040−2050.

[11] SKORPEN K G, MAULAND E, REISO O, ROVEN H J. Novel method of screw extrusion for fabricating Al/Mg (macro-) composites from aluminum alloy 6063 and magnesium granules [J]. Transactions of Nonferrous Metals Society of China, 2014, 24(12): 3886−3893.

[12] LI Y Y, WANG W H, HSU Y F, TRONG S. High-temperature tensile behavior and microstructural evolution of cold-rolled Al−6Mg−0.4Sc−0.13Zr alloy [J]. Materials Science and Engineering A, 2008, 497: 10−17.

[13] WATANABE C, JIN C Y, MONZEN R, KITAGAWA K. Low-cycle fatigue behavior and dislocation structure of an Al−Mg−Sc alloy [J]. Materials Science and Engineering A, 2004, 387: 552−555.

[14] LI Meng-jia, SHI Yun-jia, PAN Qing-lin, ZHANG Yu, LU Guang-xi, GUAN Shao-kang, BIRBILIS N. Low anisotropy of fatigue crack growth in Al−5.8Mg−0.25Sc [J]. International Journal of Fatigue, 2019, 125: 170−178.

[15] PAO P S, HOLTZ R L, JONES H N, FENG C R. Effect of environment on fatigue crack growth in ultrafine grain Al−Mg [J]. International Journal of Fatigue, 2009, 31: 1678−1683.

[16] ZHAO Hong-liang, BAI Hui-long, WANG Jun, GUAN Shao-kang. Preparation of Al−Ti−C−Sr master alloys and their refining efficiency on A356 alloy [J]. Materials Characterization, 2009, 60: 377−383.

[17] KHODABAKHSHI F, SIMCHI A, KOKABI A H, GERLICH A P. Friction stir processing of an aluminum−magnesium alloy with pre-placing elemental titanium powder: In-situ formation of an Al_3Ti-reinforced nanocomposite and materials characterization [J]. Materials Characterization, 2015, 108: 102−114.

[18] CHEN Zhong-wei, HOU Yue, XIE Bin, ZHANG Qi. Dendrite morphology evolution of Al6Mn phase in suction casting Al−Mn alloys [J]. Materials, 2020, 13: 2388.

[19] FU Jia-ni, YANG Zhao, DENG Yun-lai, WU Ye-feng, LU Jian-qi. Influence of Zr addition on precipitation evolution and performance of Al−Mg−Si alloy conductor [J]. Materials Characterization, 2020, 159: 110021.

[20] LENG Jin-feng, REN Bing-hui, ZHOU Qing-bo, ZHAO Ji-wei. Effect of Sc and Zr on recrystallization behavior of 7075 aluminum alloy [J]. Transactions of Nonferrous Metals Society of China, 2021, 31(9): 2545−2557.

[21] LI Xin-yu, XIA Wei-jun, CHEN Ji-hua, YAN Hong-ge, LI Zhen-zhen, SU Bin, SONG Min. Dynamic recrystallization, texture and mechanical properties of high Mg content Al−Mg alloy deformed by high strain rate rolling [J]. Transactions of Nonferrous Metals Society of China, 2021, 31(10): 2885−2898.

[22] CAO Cheng, ZHANG Di, WANG Xu, MA Qi-biao, ZHUANG Lin-zhong, ZHANG Ji-shan. Effects of Cu addition on the precipitation hardening response and intergranular corrosion of Al−5.2Mg−2.0Zn (wt.%) alloy [J]. Materials Characterization, 2016, 122: 177−182.

[23] ENGLER O, KUHNKE K, WESTPHAL K, HASENCLEVER J. Impact of chromium on the microchemistry evolution during solidification and homogenization of the Al−Mg alloy AA 5052 [J]. Journal of Alloys and Compounds, 2018, 744: 561−573.

[24] ASTM G67. Standard test method for determining the susceptibility to intergranular corrosion of 5XXX series aluminum alloys by mass loss after exposure to nitric acid (NAMLT Test) [S].

[25] JIANG Hai-chun, YE Ling-ying, ZHANG Xin-ming, GU Gang, ZHANG Pan, WU Yu-long. Intermetallic phase evolution of 5059 aluminum alloy during homogenization [J]. Transactions of Nonferrous Metals Society of China, 2013, 23(12): 3553−3560.

[26] GOSWAMI R, SPANOS G, PAO P S, HOLTZ R L. Precipitation behavior of the β phase in Al-5083 [J]. Materials Science and Engineering A, 2010, 527: 1089−1095.

[27] MENG Chun-yan, ZHANG Di, LIU Ping-ping, ZHUANG Lin-zhong, ZHANG Ji-shan. Microstructure characterization in a sensitized Al−Mg−Mn−Zn alloy [J]. Rare Metals, 2018, 37(2): 129−135.

[28] DING Tian, YAN Hong-ge, CHEN Ji-hua, XIA Wei-jun, SU Bin. Effect of welding speed on microstructure and mechanical properties of Al−Mg−Mn−Zr−Ti alloy sheet during friction stir welding [J]. Transactions of Nonferrous Metals Society of China, 2021, 31(12): 3626−3642.

[29] TANG Lei, PENG Xiao-yan, HUANG Ji-wu, MA Ai-bin, DENG Ying, XU Guo-fu. Microstructure and mechanical properties of severely deformed Al−Mg−Sc−Zr alloy and their evolution during annealing [J]. Materials Science and Engineering A, 2019, 754: 295−308.

[30] ZHA Min, LI Yan-jun, MATHIESEN R H, BJORGE R, ROVEN H J. Microstructure evolution and mechanical behavior of a binary Al−7Mg alloy processed by equal-channel angular pressing [J]. Acta Materialia, 2015, 84: 42−54.

[31] JIA Li, REN Xue-ping, HOU Hong-liang, ZHANG Yan-ling. Microstructural evolution and superplastic deformation mechanisms of as-rolled 2A97 alloy at low-temperature [J]. Materials Science and Engineering A, 2019, 759: 19−29.

[32] LI Jing-kun, REN Xue-ping, GAO Xiao-dan. Effect of superplastic deformation on microstructure evolution of 3207 duplex stainless steel [J]. Materials Characterization, 2020, 164: 110320.

[33] HUANG Lin-jie, QI Feng, HUA Pei-tao, YU Lian-xu, LIU Feng, SUN Wen-ru, HU Zhuang-qi. Discontinuous dynamic recrystallization of Inconel 718 superalloy during the superplastic deformation [J]. Metallurgical and Materials Transactions A, 2015, 46: 4276−4285.

[34] MENG Chun-yan, ZHANG Di, HUA Cui, ZHUANG Lin-zhong, ZHANG Ji-shan. Mechanical properties, intergranular corrosion behavior and microstructure of Zn modified Al−Mg alloys [J]. Journal of Alloys and Compounds, 2014, 617: 925−932.

[35] CARROLL M C, GOUMA P I, MILLS M J, DAEHN G S, DUNBAR B R. Effects of Zn additions on the grain boundary precipitation and corrosion of Al-5083 [J]. Scripta Materialia, 2000, 42: 335−340.

[36] YANG Yan, CHEN Yang, ZHANG Jun-xi, GU Xin-hui, QIN Peng, DAI Nian-wei, LI Xiao-peng, KRUTH J P, ZHANG Lai-chang. Improved corrosion behavior of ultrafine-grained

eutectic Al−12Si alloy produced by selective laser melting [J]. Materials & Design, 2018, 146: 239−248.

[37] DING Shi-jin, ZHANG Qing-Quang, ZHANG D W, WANG Ji-tao, ZHOU Yong-dong, LEE W W. XPS characterization of the interface between low dielectric constant amorphous fluoropolymer film and evaporation-deposited aluminum [J]. Applied Surface Science, 2001, 178: 140−148.

[38] AMOR S B, BAUD G, JACQUET M, NANSE G, FIOUX P, NARDIN M. XPS characterisation of plasma-treated and alumina-coated PMMA [J]. Applied Surface Science, 2000, 153: 172−183.

[39] KONG De-cheng, NI Xiao-qing, DONG Chao-fang, ZHANG Liang, MAN Cheng, YAO Ji-cheng, XIAO Kui, LI Xiao-gang. Heat treatment effect on the microstructure and corrosion behavior of 316L stainless steel fabricated by selective laser melting for proton exchange membrane fuel cells [J]. Electrochimica Acta, 2018, 276: 293−303.

[40] WANG Da-peng, YANG Dong, ZHANG Da-quan, LI Kang, GAO Li-xin, LIN Tong. Electrochemical and DFT studies of quinoline derivatives on corrosion inhibition of AA5052 aluminium alloy in NaCl solution [J]. Applied Surface Science, 2015, 357: 2176−2183.

[41] FANG Xu, SONG Min, LI Kai, DU Yong, ZHAO Dong-dong, JIANG Chao, ZHANG Hong. Effects of Cu and Al on the crystal structure and composition of η ($MgZn_2$) phase in over-aged Al−Zn−Mg−Cu alloys [J]. Journal of Materials Science, 2012, 47(14): 5419−5427.

[42] DAI Qing-song, DENG Yun-lai, TANG Jian-guo, WANG Yu. Deformation characteristics and strain-compensated constitutive equation for AA5083 aluminum alloy under hot compression [J]. Transactions of Nonferrous Metals Society of China, 2019, 29(11): 2252−2261.

[43] GUO M X, ZHANG Y D, YUAN B, SHA G, ZHANG J S, ZHUANG L Z, LAVERNIA E J. Influence of aging pathways on the evolution of heterogeneous solute-rich features in peak-aged Al−Mg−Si−Cu alloy with a high Mg/Si ratio [J]. Philosophical Magazine Letters, 2019, 99(2): 49−56.

[44] SOUZA P H L, QUARESMA J M V, OLIVEIRA C A S. Precipitation evolution and modeling of growth kinetics of L12-structured Al_3Zr particles in Al−0.22Zr and Al−0.32Zr (wt.%) alloys isothermally aged [J]. Materials Research, 2017, 20(6): 1600−1613.

通过添加微量元素实现的窄结晶区间 Al−2Mg−0.5Mn 合金的显微组织与性能

李梦佳[1]，张恩贵[2]，刘书玉[1]，王向东[3]，史运嘉[4]，吴建政[5]，关绍康[1]

1. 郑州大学 材料科学与工程学院，郑州 450001；
2. 贵州航天新力科技有限公司，贵州 563000；
3. 株洲中车时代电气股份有限公司 制造中心，株洲 412001；
4. 郑州大学 物理(微电子)学院 材料物理教育部重点实验室，郑州 450052；
5. 自然资源部贵金属分析与勘查技术重点实验室，郑州 450012

摘　要：Al−Mg 系合金由于大的结晶温度区间，其表面会在连铸连轧生产过程中形成较多缺陷。为了减小合金的结晶区间，研究微量 Zn、Si、Zr 和 Ti 元素对 Al−2Mg−0.5Mn 合金显微组织与性能的影响。采用 X 射线光电子能谱、原子力显微镜、扫描电镜和透射电镜对合金的显微组织进行表征。Ti 和 Zr 的添加可以在 Al−Mg−Mn 合金内部形成 Al_3Ti 和 Al_3Zr，使得其晶粒更细、强度更高，但是其结晶区间也随之变大。研究表明，添加 Zn 和 Si 能与合金内部的 Mg 形成新的第二相，从而使得共晶凝固过程中的实际 Mg 含量降低，因此，Al−2Mg−0.5Mn−0.2Zn−0.2Si 合金的结晶温度区间比 Al−2Mg−0.5Mn 合金的窄。另外，添加 Zn 和 Si 后，Al−2Mg−0.5Mn 合金的力学性能与抗腐蚀性也得到一定程度的提升。

关键词：铝镁合金；连铸连轧；力学性能；腐蚀行为；结晶温度区间

(Edited by Bing YANG)